This is a non-peer reviewed preprint submitted to EarthArXiv
It has been submitted on Oct-8, 2018 to *Geophysical Journal International*

Initiation and Arrest of Earthquake Ruptures due to Elongated Overstressed Regions

Martin Galis[1,2], Jean-Paul Ampuero[3], P. Martin Mai[4], Jozef Kristek[1,2]
1 – Comenius University in Bratislava, Slovakia
2 – Earth Science Institute, Slovak Academy of Sciences, Bratislava, Slovakia
3 – Université Côte d'Azur, IRD, CNRS, Observatoire de la Côte d'Azur, Géoazur, Nice, France
4 – King Abdullah University of Science and Technology, Thuwal, Saudi Arabia

Abstract

The initiation of natural and induced earthquakes is promoted in fault areas where the shear stress is close to fault strength. In many important situations, these overstressed fault areas (or "asperities") are very elongated; for example, in the case of a fault intersecting a reservoir subject to fluid-injection, or the stress concentration along the bottom of a seismogenic zone induced by deep fault creep. Theoretical estimates of the minimum overstressed asperity size leading to runaway rupture and of the final size of self-arrested ruptures are only available for 2D problems and for 3D problems with an asperity aspect ratio close to one. In this study, we determine how the nucleation of ruptures on elongated asperities, and their ensuing arrest, depend on the size and aspect ratio of the asperity and on the background stress. Based on a systematic set of 3D dynamic rupture simulations assuming linear slip-weakening friction, we find that if the shortest asperity side is smaller than the 2D critical length, the problem effectively reduces to a 2D problem in which rupture nucleation and arrest are controlled by the shortest length of the asperity. Otherwise, nucleation and rupture arrest are controlled by the asperity area, with a minor exception: for asperities with shortest side slightly larger than the 2D critical length, arrested ruptures are smaller than predicted by the asperity area. The fact that rupture arrest is dominantly controlled by area, even for elongated asperities, corroborates the finding that observed maximum magnitudes of earthquakes induced by fluid injection are consistent with the theoretical relation between the magnitude of the largest self-arrested rupture and the injected volume (Galis *et al.*, 2017). In context of induced seismicity, our simulations provide plausible scenarios that could be either favourable or challenging for traffic light systems, and provide mechanical insights into the conditions leading to these situations.

Keywords: Numerical modelling, Earthquake dynamics, Induced seismicity

1 Introduction

A better understanding of what controls nucleation and arrest (and thus magnitude) of earthquake ruptures is naturally important. Although theoretical models and knowledge of model parameters will probably never be accurate enough to predict when earthquakes will occur and how large they will be, analysis of theoretical models provides insight into which parameters control nucleation, growth and arrest of ruptures. Such knowledge may be particularly helpful in the context of induced seismicity, where human-controlled fluid injection is believed to be responsible for triggering earthquakes as large as M5 (e.g., Ellsworth, 2013) and measures to mitigate or avoid their hazard are being sought.

Recently, Galis *et al.*, 2017 applied a theoretical 3D model of rupture arrest to induced seismicity. They considered earthquakes initiated over a limited fault area (hereafter referred to as an *asperity*), weakened by an increased pore fluid pressure, to investigate how large ruptures may grow. They found a very good agreement between their model predictions (in particular estimated magnitude of the largest arrested rupture as a function of volume of injected fluids) and observed magnitudes of the largest earthquakes induced by fluid injection over a broad range of scales (from laboratory experiments to large field operations). The largest arrested rupture is defined as the largest rupture that stops spontaneously by lack of available elastic energy, rather than by encountering a strong barrier. Larger events, so called runaway ruptures thatpropagate until stopped by a sufficiently strong barrier, are still possible. In their study, Galis *et al.*, 2017 only considered asperities of aspect ratio close to 1. However, reservoirs are often much thinner in the vertical direction than horizontally, thus their intersection with sub-vertical faults is elongated in the sub-horizontal direction, which leads to asperitiy aspect ratios far from 1 (Fig 1A).

Elongated overstressed regions also important for natural earthquakes, in particular for ruptures nucleated by stress concentrations along the bottom of the seismogenic zone, where stresses are concentrated by aseismic slip on the deeper portions of the fault (Fig 1B). The presence of stress concentration near transitions of fault rheology are a mathematical result of the theory of dislocations in elastic media (e.g. Kato, 2012; Bruhat and Segall, 2017) and are a typical result of interseismic stress calculations based on geodetically-derived seismic coupling maps (Ader *et al.*, 2012) or long-term slip rates (Mildon *et al.*, 2017). Ruptures that nucleated on deep stress concentrations may remain confined at depth without breaking the

entire fault width like, for example, the 2015 M7.8 Gorkha, Nepal earthquake (Avouac *et al.*, 2015; Michel *et al.*, 2017). Such partial ruptures may be examples of self-arrested ruptures that precede a larger event (Galis *et al.*, 2017). Stress concentrations play an important role also in some induced seismicity situations. Notably, in producing gas fields, peaked stresses can develop along the top or bottom of the intersection between the reservoir and a fault, due to the effect of differential compaction between reservoir compartments that are offset by the fault (Mulder, 2003; Buijze *et al.*, 2017; Van Wees *et al.*, 2017).

Motivated by these considerations, our study focuses on the nucleation and arrest of earthquake ruptures due to elongated asperities. Our results extend and complement previous research on rupture nucleation and arrest based on fracture mechanics (e.g., Ampuero *et al.*, 2006; Ripperger *et al.*, 2007; Galis *et al.*, 2015) including those developed in the context of induced seismicity but limited to 2D (Garagash and Germanovich, 2012; Dempsey and Suckale, 2016; Azad *et al.*, 2017) or to 3D with asperity aspect ratio near 1 (Galis *et al.*, 2017).

The nucleation and arrest of ruptures due to asperities with aspect ratio close to one has been shown to be controlled by asperity area (Galis *et al.*, 2015, 2017). However, in the limit of an asperity with infinite or zero aspect ratio, a 3D problem reduces to a 2D problem, which is controlled by asperity length. Previous works studying the conditions leading to the onset of slip instabilities in 3D (Uenishi, 2009, 2018) already reported such transition, but did not examine whether the resulting rupture is self-arrested or runaway. Therefore, although the ruptured area of arrested ruptures and the conditions leading to runaway ruptures for elongated asperities have not been yet described by theoretical/analytical solutions (at least we are not aware of it), we expect these rupture properties to display a transition from an area-controlled behaviour to a length-controlled behaviour.

Here, we develop a synoptic understanding of the propagation and arrest of ruptures nucleated by elongated asperities, based on numerical simulations and theoretical developments. The remainder of this paper is organized as follows. In Sections 2 and 3 we analyse the conditions required to generate runaway ruptures and the size of arrested ruptures, respectively. In Section 4 we present the implications of our results for a specific case of asperities with fixed width or length, especially in the context of induced seismicity. In Section 5 we briefly discuss the case of oblique orientation of an asperity with respect to

the initial traction. The Appendices present a derivation of critical lengths for runaway rupture in 2D and their verification using numerical simulations.

2 Nucleation of runaway ruptures

Here we investigate the conditions that lead to runaway ruptures for asperities of arbitrary aspect ratio. Galis *et al.*, 2015 studied conditions for runaway ruptures in 3D for asperities with aspect ratio close to one. For high background stress they found that an asperity area greater than that estimated by Uenishi, 2009, 2018 for elliptical asperities leading to self-accelerating slip, is also sufficient to produce runaway ruptures. For lower levels of background stress, after onset a rupture either arrests spontaneously or becomes runaway;in this context, Galis *et al.*, 2015 derived a new estimate of the critical area leading to runaway ruptures. Because of the expected transition from an area-controlled 3D problem to length-controlled 2D problem, we here first derive 2D estimates of critical length that are physically consistent with the 3D estimates of critical area by Galis *et al.*, 2015. Then, we compare our numerical results for elongated asperities with the 2D and 3D theoretical estimates. Finally, we propose a general procedure to estimate whether an elongated asperity will produce a runaway or self-arrested rupture.

We followed the approach of Galis *et al.*, 2015 and derived theoretical estimates of a "critical length" for 2D problems, defined as the minimum asperity length that can produce runaway ruptures. The critical length is defined as $a_c = \max(a_{UR}, a_2)$, where a_{UR} is the estimate by Uenishi and Rice, 2003, and a_2 is our estimate derived in Appendix A. We verified the estimate a_c using numerical simulations (Appendix B). The critical length a_c depends on strength parameter $S = (\tau_s - \tau_0)/(\tau_0 - \tau_d)$, where τ_0 is the initial background shear traction, and τ_s and τ_d are static and dynamic friction strengths, respectively. For low S (i.e., high background stress) the critical length a_c for mode II (in-plane) and III (anti-plane) is determined by a_{UR}, which does not depend on S (Fig B1). For greater S (i.e., low background stress), the critical length a_c is determined by our estimate a_2, which grows with increasing S. The transition between these two regimes occurs at $S \approx 2.75$. This behaviour

is qualitatively consistent with 3D results by Galis *et al.*, 2015, but in 3D the transition occurs at $S \approx 0.75$. Such difference in critical values for 2D and 3D problems is not surprising and has been observed, for example, for the transition to super-shear rupture via the daughter-crack mechanism (e.g., Dunham, 2007).

Because there is no analytical estimate of the critical area of an elongated asperity, we performed numerical simulations with elongated asperities for a wide range of aspect ratios. For the simulations, we used the finite-element method (e.g., Moczo *et al.*, 2014) and a regular mesh, with the fault being discretized by square elements. To achieve an exact discrete-mesh geometrical representation of the asperity, we consider a rectangular asperity. In the numerical simulations, we used the same parameters as for the verification of the 2D estimates (Table B1). By varying the initial traction τ_0 we obtained S values of 0.1., 0.5, 1, 1.5, 2, 3 and 4. We considered a fixed ratio between overstress and strength excess (0.5%) and asperities with aspect ratios ranging from 1:30 to 50:1. The aspect ratio 1:1 corresponds to a square, 5:1 to a rectangle elongated in the mode II direction and 1:5 to a rectangle elongated in the mode III direction (Fig 2A). All the results are plotted using length and area normalized by L_{fric} and L_{fric}^2, respectively, where $L_{fric} = \mu . D_c / (\tau_s - \tau_d)$ is the characteristic length scale induced by slip-weakening friction (e.g. Ampuero *et al.*, 2002; Dunham, 2007).

The critical conditions at the transition to runaway ruptures in our simulations are identified as follows. For each individual numerical simulation, we consider an asperity with fixed size and overstress and we evaluate whether the resulting rupture stopped propagating spontaneously at a finite distance (self-arrested rupture) or whether it propagated across the entire fault plane (runaway rupture). Our numerical results are summarized in Fig 2B. To visualize the critical conditions, empty symbols depict the largest asperity producing the largest arrested rupture and filled symbols denote the smallest asperity producing a runaway rupture. For better visualization of the transition, we considered asperities with aspect ratios close to several predefined/discrete values (1:30, 1:25, etc). For cases with $S \leq 2$, a 30 km x 15 km fault is sufficient to contain the largest arrested ruptures, however, for $S = 3$ and $S = 4$ we used faults with dimensions up to 60 km x 30 km to accommodate not only the largest arrested ruptures but also asperities with extreme aspect ratios.

Our simulations confirm that the transition to runaway ruptures follows mainly two regimes, depending on asperity aspect ratio. For aspect ratio 1:1, the numerical results are consistent with the theoretical criterion based on critical area by Galis *et al.*, 2015 (bold lines in Fig 2B). For intermediate aspect ratios (e.g., ranging from 1:4 to 8:1 for $S = 2$), an *area-controlled regime* prevails: the runaway transition is controlled by the same critical area criterion as for a square asperity (1:1). For more elongated asperities (e.g., aspect ratios smaller than 1:8 and larger than 14:1 for $S = 2$), we find a *length-controlled regime*: the runaway transition occurs when the narrower side of the asperity exceeds the 2D critical length (Appendix A), regardless of asperity area. The critical lengths are consistent with the corresponding 2D theoretical estimates in both mode II and III directions (thin lines in Fig 2B). The range of aspect ratios in the area-controlled regime grows with increasing S, especially when $S < 2$. The two regimes show asymptotic behaviour; the transition between them is rather sharp for $1 \le S \le 2$ but more gradual for $S = 0.5$. Theory predicts that in 3D the critical area depends on S if $S > 0.75$, whereas in 2D the critical length grows with S if $S > 2.75$. This explains why in Fig 2B, for $1 \le S \le 2$, the runaway transitions coalesce in the length-controlled regime but are separated in the area-controlled regime; and for $S = 3$ and $S = 4$, the runaway transitions are separated also in the length-controlled regime. The deviation from the theoretical estimates for $S = 0.1$ and $S = 0.5$ - for which the numerical results indicate a larger critical area than the theoretical estimate - is a consequence of numerical artefacts of the rectangular asperity, reported previously by Galis *et al.*, 2015, who observed relatively slow convergence of the critical area for the square asperity, particularly for $S < 0.75$ (see their Fig 9). They observed the fastest convergence for an elliptical asperity with aspect ratio 4:3. However, a stair case representation of an ellipse in a regular mesh requires a very small element size for a proper geometrical representation of elongated asperities, which would lead to prohibitively large computational costs for our parametric study.

Based on these results, in particular on the agreement between theory and simulation in the dependence of the runaway transition on S, we conclude that the transition to runaway ruptures is controlled either by i) the critical area if the narrower side of the asperity is greater than the corresponding 2D estimate of the critical length, or ii) by the critical length. We propose the following procedure to determine whether an elongated asperity (with area

$A = a \times b$, and aspect ratio $\alpha = a / b$; a and b are the lengths of the asperity in mode II and III directions, respectively) will produce a runaway or an arrested rupture:

1) For given S value, estimate critical area, A_{crit}, following Eq. 26 of Galis *et al.*, 2015.

2) For given S value, estimate critical lengths a_{crit} and b_{crit} for modes II and III, respectively (Eq. A14 in Appendix A).

3) Determine the smallest and largest aspect ratios for the area-controlled regime

$$\alpha_{\min} = \frac{a_{crit}^2}{A_{crit}} \quad \text{and} \quad \alpha_{\max} = \frac{A_{crit}}{b_{crit}^2}$$

4) If $\alpha_{\min} < \alpha < \alpha_{\max}$, the asperity aspect ratio falls into the area-controlled regime and the rupture is

a) runaway if $A > A_{crit}$,

b) arrested if $A \le A_{crit}$.

5) Otherwise, the asperity aspect ratio falls into the length-controlled regime and the rupture is

a) runaway if $L > L_{crit}$

b) arrested if $L \le L_{crit}$

where L and L_{crit} denote a and a_{crit} if $\alpha < \alpha_{\min}$, or b and b_{crit} if $\alpha_{\max} < \alpha$.

Steps 3 to 5 can be more succinctly expressed as follows. Ruptures are runaway if the following three conditions are met simultaneously: $A > A_{crit}$, $a > a_{crit}$ and $b > b_{crit}$. Otherwise, ruptures are arrested. These approximate conditions define each runaway boundary in Fig. 2 by three straight lines. The true boundaries may have some curvature near the transition between the area-controlled and length-controlled regimes. Such curvature is visible in Fig. 2 for the numerical simulations for the two largest values of S.

3 Extent of arrested ruptures

In the previous section, we investigated the conditions leading to runaway ruptures. Now, we are interested in estimating the size of self-arrested ruptures, and in particular its dependence on asperity aspect ratio.

Previous 2D and 3D results provide final rupture sizes for end member cases of asperity aspect ratios, but also suggest that the intermediate cases may be non-trivial. In 2D, Ampuero and Ben-Zion, 2008 (their Appendix B) applied fracture mechanics theory to estimate the final length of self-arrested arrested ruptures as a function of asperity length. In 3D, Galis *et al.*, 2017 used a similar approach to estimate the final rupture area. For asperities with aspect ratios close to one, they found that ruptured area is controlled by asperity area. The theoretical estimates derived by the two studies were supported by simulation results and complement each other. Considering a wider range of asperity aspect ratios in 3D, just like for the runaway transition, we expect a transition from purely 3D behaviour (area-controlled) for asperities with aspect ratio close to one, to 2D behaviour (length-controlled) for extremely elongated asperities. However, in 2D, arrested ruptures occur for $S > 2.75$, whereas in 3D and for asperities with aspect ratio close to one, they occur already for $S > 0.75$. This suggests that aspect ratio has a more complex effect on rupture arrest than on the runaway transition.

Our new simulations provide a comprehensive picture of the effects that the asperity aspect ratio has on rupture arrest. To allow better coverage of the arrested ruptures, we performed additional simulations,in addition to those included in Fig 2. The results are summarized in Fig 3. Each row shows results for a fixed S value, ranging from 1 to 4. Results for $S = 0.1$ and $S = 0.5$ are not shown, because arrested ruptures exist only for $S > 0.75$. Overall, by comparing the numerical results with 2D and 3D theoretical estimates, we identify three regimes: rupture arrest controlled by asperity length (squares), by asperity area (circles), and by neither length nor area (diamonds).

Our simulations confirm that the end-member regimes of rupture arrest are consistent with theoretical expectations. In the area-controlled regime of rupture arrest, for all aspect ratios, we find almost perfect agreement between the numerically simulated and theoretically predicted areas of arrested ruptures (yellow circles and yellow curves, respectively, in the left column of Fig 3). In this regime, the runaway transition is also area-controlled.

In the length-controlled regime of rupture arrest (which exists only for $S > 2.75$) the final rupture size is consistent with the theoretical estimates for mode II and mode III, depending on the orientation of the elongated asperity (squares and curves of corresponding colours in Figs 3B and 3E). The agreement is, however, not as perfect as in the area-controlled regime. This could be affected by prevailing 3D effects or non-zero stress drop. Although the asperities

in the length-controlled regime are very elongated, they are finite and 3D effects may still affect rupture propagation. This would imply smaller discrepancies for more elongated asperities, which are better approximations of a 2D problem. Because we do not observe such behaviour, we conjecture that the observed deviations are caused by non-zero stress drop (i.e, $\tau_0 - \tau_d > 0$). Ampuero and Ben-Zion, 2008 observed almost perfect agreement between 2D predictions and simulations of arrest size only for $\tau_0 - \tau_d = 0$, whereas in all our simulations $\tau_0 - \tau_d > 0$. Finally, for all our cases in the length-controlled regime of rupture arrest, the runaway transition is also length-controlled.

The most interesting regime is the third one, which we identified for $S > 1.5$ (diamonds in Fig 3). In this non-trivial regime, the simulated arrest sizes are not consistent with theoretical predictions, even though the transition to runaway ruptures is. While the length of asperities in this group is in a range where 2D estimates predict runaway ruptures, the asperities still produce arrested ruptures (middle column of Fig 3). Moreover, the arrest area is smaller than predicted by the 3D estimate (left column of Fig 3). The fact that neither asperity area nor length describe this group sufficiently well suggests that rupture arrest may be controlled by mixed mode II+III rupture. In our simulations the asperities sides are parallel or perpendicular to the orientation of initial traction. For asperities with aspect ratio close to one or for very elongated asperities this makes no difference, because rupture nucleation and arrest are controlled by area or length, respectively. However, for the intermediate regime, the effect of area is no longer sufficient and the effect of length is not yet strong enough. Therefore, we conjecture that in this range the mixed mode II+III plays an important role in rupture nucleation and arrest. This also suggests that the role of mixed mode could be important for cases with oblique orientation between the asperity and initial traction. We will briefly discuss this aspect in Section 5.

We propose the following general procedure to estimate the area of arrested ruptures, A_{arr}, nucleated by an elongated asperity. This procedure cannot be used to estimate the size of runaway ruptures, which is generally controlled by barriers and fault geometry.

1) Determine whether the asperity produces arrested ruptures (Section 2). If it does, continue.

2) If $2\alpha_{\min} < \alpha < \alpha_{\max}/2$, the asperity aspect ratio falls into the area-controlled regime. Then:
    a. rupture is bounded by the asperity size, hence $A_{arr} = A$, if
        i. $S < 0.75$,

        or

        ii. $S > 0.75$ and $A < A_U$, where A_U is the critical asperity area leading to self-accelerating slip derived by Uenishi, 2009, 2018
    b. Otherwise, rupture is arrested outside the asperity. Then A_{arr} can be estimated following Galis *et al.*, 2017
3) If $\alpha < \alpha_{\min}$ or $\alpha_{\max} < \alpha$, the aspect ratio falls into the length-controlled regime. Then:
    a. rupture is bounded by the asperity, hence $A_{arr} = A$, if
        i. $S < 2.75$,

        or

        ii. $S > 2.75$ and $L < L_{UR}$, where L_{UR} is the critical asperity length leading to self-accelerating slip derived by Uenishi and Rice, 2003), for the corresponding mode (II or III)
    b. otherwise, the rupture propagates outside the asperity. The distance at which rupture is arrested, L_{arr}, can be estimated following Ampuero and Ben-Zion, 2008. To estimate the ruptured area, A_{arr}, we can assume an elliptical rupture with minor semi-axis equal to L_{arr} and major semi-axis determined by the half-length of the asperity.
4) If $\alpha_{\min} < \alpha < 2\alpha_{\min}$ or $\alpha_{\max}/2 < \alpha < \alpha_{\max}$, the aspect ratio falls into the intermediate regime. The rupture area A_{arr} obtained following the steps for the area-controlled regime (step 2) can be considered a conservative estimate.

Note that the factor 2 used above to limit the intermediate regime is an approximation, based on numerical results.

4 Asperity with fixed width or length

In previous sections, we considered an asperity of a given size and investigated the rupture size it can produce. However, in nature, asperities grow in time. In a fluid-injection context, the fault region affected by fluid pressure and poroelastic stress perturbations expands as injection progresses. In a tectonic context, the spatial extent of the stress concentration near the edge of a locked fault area increases due to creep in the unlocked area. One dimension of the growing overstressed area may be constrained, for example by the thickness of the pressurized reservoir. Having this interpretation in mind, we will now discuss the special case of an asperity with fixed width or length but increasing area, with potentially important implications for fluid injection operations.

We note that, when simulating ruptures on asperities of a given size, we have not accounted for the possibility that the asperity may have produced ruptures previously (seismic or aseismic) when it was still smaller. In particular, we neglected any stress redistribution caused by such previous events. Thus, our estimate of the size of arrested ruptures can be considered as an upper bound for a given asperity size.

The results presented in Fig 2 are valid for any asperity. The length a and width b have to be compared with the critical curve corresponding to the given S-value. As shown in the conceptual figure (Fig 4), if the asperity dimensions fall below the critical curve, the asperity produces an arrested rupture (either asperity-bounded or arrested outside of the asperity), otherwise it produces a runaway rupture. Faults producing arrested ruptures lead to smaller earthquake magnitudes, and thus pose less hazard than faults producing runaway ruptures. If a and b are far from a_{crit} and b_{crit}, respectively, the system behavior is relatively predictable, it is only mildly affected by small changes of a or b. However, this picture changes if a or b are close to their critical values. This is better seen using examples.

We first illustrate the transition to runaway rupture for an asperity with fixed width b and growing length a. Increasing its area moves it along a horizontal line in Figs 2B or 4. If b is far from b_{crit}, the system's behavior is relatively predictable. On the other hand, if b is close to b_{crit}, the system becomes very sensitive to b. We illustrate this behavior using numerical simulations, described in terms of dimensional values for width and length; however, note that these are only valid for our particular choice of parameter values. We consider $S = 4$

and a fixed and slightly overcritical width b (corresponding to Scenario 1 in Fig 4). Here, the critical sizes are $a_{crit} = 1.31$ km and $b_{crit} = 0.98$ km. The simulation results in Fig 5A show that an asperity with length a = 1.35 km produces ruptures bounded in all directions by the asperity. Increasing a to 2.6 km leads to self-arrested ruptures that propagate outside the asperity, mostly in the vertical direction, while their horizontal size remains constrained by the asperity length. Their rupture size grows with growing a. Eventually, if a=42 km, above the critical length, the fault produces runaway ruptures.

We now consider an asperity with fixed length a and growing width b. Increasing its area moves it along a vertical line in Figs 2B or 4. We consider again $S = 4$, set a=42 km (a value producing runaway rupture), and then vary b (corresponding to Scenario 2 in Fig 4). As shown by our numerical simulations (Fig 5B), an asperity with b=0.75 km (and narrower) produces ruptures bounded by the asperity while an asperity with b=1.05 km (and wider) already produces a runaway rupture. At intermediate values of b, ruptures propagate outside the asperity in the vertical direction and then self-arrest.

Both sets of examples can be viewed as approximations of two scenarios of fluid injection into a reservoir bounded by impermeable layers and intersected by a fault. The first scenario is injection into a laterally extended reservoir with no fluid migration along the fault. The second case corresponds to fluid-injection into a saturated reservoir with fluid migration along the fault plane. As indicated in Fig 4, in the first scenario, the system produces arrested ruptures that propagate outside the asperity for a very broad range of asperity lengths (a from 1.35 to 42 km). In contrast, in the second scenario this occurs only for a narrow range of asperity widths (roughly b from 0.75 to 1.05 km), where even relatively small changes in width are sufficient to dramatically affect the rupture behavior. Here we considered a low initial shear stress ($S = 4$), for which arrested ruptures exist even in the length controlled regime. However, faults with higher initial stress levels ($S < 2.75$) do not produce arrested ruptures in the length controlled regime (Appendix A), and thus, there would be a direct transition from ruptures bounded by the asperity to runaway ruptures in the second scenario.

These idealized examples reveal important implications for traffic light systems (TLSs), used to monitor fluid-injection operations. In the first scenario, regardless of the tectonic stress level, arrested ruptures would happen during a relatively long period of injection with sizes

growing significantly before the transition to runaway rupture occurs. This progressive evolution towards runaway rupture could potentially provide enough time for TLS to detect it, and for operators to respond to prevent a runaway rupture. However, in the second scenario and at high tectonic-stress level ($S < 2.75$), the absence of arrested ruptures eliminates a potential precursor to runaway ruptures, which poses a particular challenge for TLSs. Additionally, higher permeability along a fault together with the sensitivity of the system to relatively mild changes of the width b imply that the transitions from asperity-confined ruptures to ruptures self-arrested outside the asperity, to runaway ruptures could occur faster in the second scenario than in the first one, posing another challenge for TLSs.

5 Oblique orientation of initial stress and asperity

In the previous analysis, we considered asperities oriented either parallel or perpendicular to the initial shear traction (Fig 2A). A complete analysis of cases with oblique orientation is beyond the scope of this paper. However, we expect qualitatively similar results, in particular the runaway transition should also be controlled by either asperity area or length, depending on asperity aspect ratio, although possibly with different values of critical area and critical length. Ripperger *et al.*, 2007 studied ruptures on faults with stochastic heterogeneous stress distributions, which resulted in asperities of irregular shape. They found that rupture nucleation was achieved if the radius of the inscribed circle of the irregular asperities exceeded a critical nucleation length. Similarly, for oblique stress-asperity orientations, we conjecture that runaway ruptures occur if the inscribed ellipse with major axis oriented parallel to the initial traction has major and minor axes larger than the critical lengths a_{crit} and b_{crit}, respectively, and its area is larger than A_{crit}.

To test our conjecture, we performed three simulations with $S = 4$, aspect ratio 50:1 and initial traction rotated by 45°with respect to the asperity (Fig 6). In the first simulation, we set an asperity size leading to runaway rupture if τ_0 is oriented parallel to the asperity elongation (a=52.5 km and b=1.05 km). Under oblique initial stress, the asperity is too narrow to include the critical ellipse determined by a_{crit} and b_{crit} (Fig 6A) and, as expected, it produced an arrested rupture (Fig 6B). In the second simulation we set b=1.15 km. In this case, the asperity

is slightly narrower than the critical ellipse and also produced an arrested rupture. In the third simulation, we set b=1.2 km. The asperity is now wide enough to include the critical ellipse and, as expected, it produced a runaway rupture.

Although the results of these limited numerical tests are consistent with our expectations, a detailed parametric study, investigating various orientations, aspect ratios and S -values, has to be performed to confirm our conjectures. We leave such a study for future work.

6 Conclusions

We studied how elongated overstressed asperities hosting earthquake initiation affect rupture nucleation and arrest. Problems with very elongated asperities reduce to a 2D problem. For low values of strength parameter S (i.e., for high background stress level), the critical length for runaway ruptures is independent of S, in this case, the large-scale-yielding estimates by Uenishi and Rice, 2003 are sufficient. If $S > 2.75$, the critical length depends on S, for which we derived small-scale-yielding analytical estimates and verified them against results of numerical simulations. Galis *et al.*, 2015 observed a similar transition in 3D between large- and small-scale-yielding regimes, but at a lower critical value of $S \sim 0.75$.

Because a theoretical analysis of ruptures nucleated on elongated asperities is not available, we have performed a parametric study using numerical dynamic rupture simulations. We found that the transition to runaway ruptures is controlled by either asperity length or asperity area, depending on aspect ratio and background stress. The transition between the two regimes is narrow. We proposed a procedure to determine whether an asperity will produce an arrested or a runaway rupture.

We further investigated the size of arrested ruptures and compared results of numerical simulations with 2D and 3D theoretical estimates of rupture arrest size (Ampuero and Ben-Zion, 2008; Galis *et al.*, 2017). Rupture arrest follows three separate regimes depending on asperity aspect ratio and background stress: a *length-controlled regime*, in which final rupture size is well predicted by 2D estimates by Ampuero and Ben-Zion, 2008; an *area-controlled regime*, in which final rupture area follows the 3D estimates by Galis *et al.*, 2017; and a *mixed regime* in which the rupture arrest is controlled neither by asperity length nor by area. In the

last case, no analytical estimate of the final rupture size is available, but an upper bound is provided by Galis *et al.*, 2017.

The core of our analysis focused on asperities aligned with or perpendicular to the initial fault shear traction. Under oblique orientation of stress with respect to the asperity, we hypothesized that runaway ruptures occur if both axes of the asperity-inscribed ellipse with major axis oriented parallel to the initial traction are larger than the critical lengths and its area is larger than the critical area. Results of a limited set of simulations supported this hypothesis.

In the context of induced seismicity, our idealized model results provide scenarios that could be either favourable or challenging for traffic light systems (TLSs), and allow to gain insights into the mechanical conditions leading to them. Situations with a progressive transition from arrested to runaway ruptures, involving events of growing size over an extended period, constitute the best-case scenario for a TLS. A sudden or very narrow transition to runaway rupture, a challenging situation for a TLS, may occur on very elongated asperities with shorter dimension close to the critical size for runaway rupture (variations of the longer asperity side have only limited effects).

Acknowledgments

The research reported in this publication was supported by funding from King Abdullah University of Science and Technology (KAUST), grant BAS/1/1339-01-01. M.G. and J.K. acknowledge partial support by the Slovak Foundation Grant VEGA-2/0188/15. J. P. A. acknowledges partial funding from NAM (Nederlandse Aardolie Maatschappij) and from the French government through the UCA-JEDI Investments in the Future project managed by the National Research Agency (ANR) with the reference number ANR-15-IDEX-01.

Appendix A: Critical lengths for 2D runaway ruptures

Here we derive estimates of critical lengths for runaway ruptures on 2D faults based on the Griffith crack equilibrium criterion and small-scale-yielding fracture mechanics, valid at low

background stress levels. Then, in combination with known large-scale-yielding nucleation lengths, we provide a critical length estimate valid at all stress levels.

Adopting the approach of Galis *et al.*, 2015 (Appendix A),Ripperger *et al.*, 2007 (Appendix B) and Azad *et al.*, 2017, we assume an overstressed asperity with half-length a_i with stress τ_i (greater than the static friction τ_s). The static stress intensity factor for symmetric non-uniform stress drop is (Ampuero *et al.*, 2006)

$$K_0(a) = \sqrt{\pi a}\,\frac{2}{\pi}\int_0^a \frac{\Delta\tau(x)}{\sqrt{a^2 - x^2}}\,dx \ , \tag{A1}$$

where a is the crack half-length and $\Delta\tau$ the stress drop. The criterion for crack arrest is

$$\eta K_0 \le K_c \, , \tag{A2}$$

where η is an adjustable factor to account for effects of overshoot (Galis et al., 2015). We calibrate its value numerically (Appendix B). Assuming linear slip-weakening friction, K_c may be approximated as

$$K_c^2 = 2.\mu^* G_c = \mu^*.D_c.\left(\tau_s - \tau_d\right), \tag{A3}$$

where D_c is the characteristic slip-weakening distance, τ_s and τ_d are static and dynamic frictional strengths, respectively, and $\mu^* = \mu$ for mode III or $\mu^* = \mu/\left(1-\nu\right)$ for mode II, where μ is shear modulus and ν is Poisson's ratio.

A first estimate of the critical size for runaway rupture is derived assuming $a_i << a$. The effect of an overstressed asperity on a fault with uniform background stress τ_0 can then be represented using a point-load approximation as

$$\Delta\tau(x) = \Delta\tau_0 + F.\delta(x) \, , \tag{A4}$$

where $\Delta\tau_0 = \tau_0 - \tau_d$ is the background stress drop, $\delta(x)$ is the Dirac delta function and $F = \frac{1}{2}a_i.\left(\tau_i - \tau_0\right)$ is the force due to excess stress on the asperity. Eq. (A1) then yields

$$K_0(a) = \Delta\tau_0\sqrt{\pi a} + \frac{2F}{\sqrt{\pi a}} \ . \tag{A5}$$

This function has a single minimum, $K_0^{\min} = \sqrt{8.F.\Delta\tau_0}$. The condition for runaway rupture, obtained by negating the condition in Eq. A2, is then

$$\eta K_0^{\min} > K_c \ . \tag{A6}$$

By solving Eq. (A6) for a_i we find the first-order condition for runaway rupture

$$a_i > a_1' = \frac{1}{\eta^2}\frac{\mu^*.D_c.(\tau_s - \tau_d)}{8.(\tau_i - \tau_0).(\tau_0 - \tau_d)} \ . \tag{A7}$$

A more accurate estimate is derived now. For arbitrary values of $a_i < a$, eq. (A1) yields

$$K_0(a) = \sqrt{\pi a}\,(\tau_0 - \tau_d)\left[1 + \frac{\tau_i - \tau_0}{\tau_0 - \tau_d}\frac{2}{\pi}\arcsin\left(\frac{a_i}{a}\right)\right]. \tag{A8}$$

The condition for runaway rupture, Eq. (A6), can no longer be solved analytically for a_i . To facilitate numerical solution, we introduce the function

$$f(x,\gamma) = \sqrt{x}\left[1 + \frac{2\gamma}{\pi}\arcsin\left(\frac{1}{x}\right)\right] \tag{A9}$$

and rewrite Eq. (A8) as

$$K_0(a) = \sqrt{\pi a_i}\,(\tau_0 - \tau_d)\,f(a/a_i,\gamma), \tag{A10}$$

where $\gamma = (\tau_i - \tau_0)/(\tau_0 - \tau_d)$. The stress intensity factor has a single minimum

$$K_0^{\min} = \sqrt{\pi a_i}\,(\tau_0 - \tau_d)\,f_{\min}(\gamma), \tag{A11}$$

where $f_{\min}(\gamma) = \min_x f(x,\gamma)$ is computed numerically. Solving Eq. (A6) then yields

$$a_i > a_2' = \frac{1}{\eta^2}\frac{\mu^*.D_c.(\tau_s - \tau_d)}{\pi.(\tau_0 - \tau_d)^2.f_{\min}^2(\gamma)} \ . \tag{A12}$$

Eqs. (A7) and (A12) are derived for half-lengths. However, in the main part of the paper we find it more convenient to work with the full asperity length. We thus define the critical length, in the small-scale yielding regime, as $a_2 = 2a_2'$.

The critical length a_2 depends on the strength parameter $S = (\tau_s - \tau_0)/(\tau_0 - \tau_d)$. As found in 3D by Galis *et al.*, 2015 and in 2D by Azad *et al.*, 2017, the estimate a_2 is valid for low background stress (high values of S), whereas at high stress (low S) the critical length is the large-scale-yielding estimate of nucleation size by Uenishi and Rice, 2003

$$a_{UR} \cong 1.158\,\mu^* \frac{D_c}{\tau_s - \tau_d} \tag{A13}$$

Our final estimate of the critical size for runaway rupture in 2D, valid for all values of S, is

$$a_c = \max(a_{UR}, a_2)\,. \tag{A14}$$

Fig A1 shows this estimate as a function of S.

Additionally, Fig A1 indicates the location of three rupture regimes in parameter space (S, $a\ /L_{fric}$). The critical length a_{UR} by Uenishi, 2009, 2018 is the minimum asperity length for the onset of slip instability. Asperities smaller than a_{UR} produce ruptures that stop quickly and remain contained inside the asperity. Asperities larger than a_{UR} produce runaway ruptures in high background stress (low S) environments. At low background stress, asperities larger than a_{UR} produce ruptures that stop spontaneously outside the asperity, and asperities larger than a_2 produce runaway ruptures.

Appendix B: Verification and calibration of the theoretical estimates of critical lengths

Here we summarize results of our numerical tests to determine the value of the adjustable parameter η and the regions of applicability of $a_1 = 2a_1'$, a_2 and a_{UR} estimates. We utilized two implementations of the spectral boundary integral equation method for 2D rupture dynamics (Morrisey and Geubelle, 1997; Cochard and Rice, 2000; Lapusta *et al.*, 2000), the BIMAT-PCSI code for mode II rupture (Rubin and Ampuero, 2007; Ampuero, 2008a) and the SBIEMLAB code for mode III rupture (Ampuero, 2008b). In both cases, we used a spatial discretization of 14.65 m, which is 40 times smaller than the static process zone size $\Lambda_0 = 617$ m, which we found to be largely sufficient for proper numerical resolution of dynamic rupture problems with slip-weakening friction (Day *et al.*, 2005). To accommodate varying strength

parameter S, we considered fixed values of static and dynamic frictional strength, τ_s and τ_d, and variable initial shear traction τ_0. All parameter values are summarized in Tab. B1. Additionally, we considered three overstress levels in the asperity – low, medium and high, corresponding to 0.00005%, 0.5% and 5% of the strength excess, ($\tau_s - \tau_0$), respectively.

The results of our numerical simulations are summarized and compared with the theoretical estimates in Fig B1. First, we discuss the cases of low and medium overstress, which lead to very similar results. For $S > 2.5$, the numerical results are consistent with the theoretical estimates a_1 and a_2, whereas for $S \le 2.5$ they are consistent with the estimate a_{UR}. These results confirm the applicability of the estimate of the critical length a_c given in Eq. (A14). We also confirm that the S-value at which the critical asperity size becomes S-dependent ($S = 2.87$), is greater than in 3D ($S \approx 0.75$). For high overstress and $S > 2$, our estimates a_1 and a_2 are consistent with the numerical results. However, for $S < 2$ the critical length obtained numerically is smaller than a_{UR}. The reason is that the estimate a_{UR} has been derived without considering overstress. This deviation is thus expected; and it is consistent with 3D results presented by Galis et al., 2015. Although the overstress is relatively high, 5% of the strength excess, it varies only from 80 kPa for $S = 0.1$ to 600 kPa for $S = 2$, which are values within the expected range of effects of pore pressure in the context of induced seismicity.

We used the comparison of the theoretical estimates a_1 and a_2 with numerical results also to calibrate the adjustable factor η. Through trial-and-error we find that $\eta = 1.04$ ($1/\eta^2 = 0.925$) yields consistent results for mode II and III ruptures in the considered range of overstress levels.

The value of S at the transition between small- and large-scale-yielding regimes depends slightly on the overstress (Fig B1). The exact value can be obtained from the condition $a_2 = a_{UR}$. Although the exact value for low to medium overstress is $S = 2.87$, numerical results suggest (Fig 1B) that it ranges from 2.5 to 3. Therefore, in the main text we refer to the transition value as $S \approx 2.75$. Galis *et al.*, 2015 observed qualitatively the same transition in 3D, but at a lower value $S \approx 0.75$, obtained from the condition $A_2 = A_U$.

References

Ader, T., Avouac, J.-P., Liu-Zeng, J., Lyon-Caen, H., Bollinger, L., Galetzka, J., Genrich, J., Thomas, M., Chanard, K., Sapkota, S. N., Rajaure, S., Shrestha, P., Ding, L. and Flouzat, M. (2012) 'Convergence rate across the Nepal Himalaya and interseismic coupling on the Main Himalayan Thrust: Implications for seismic hazard', *Journal of Geophysical Research: Solid Earth*. Wiley-Blackwell, 117(B4), p. n/a-n/a. doi: 10.1029/2011JB009071.

Ampuero, J.-P. ., Vilotte, J.-P. . and Sánchez-Sesma, F. J. . (2002) 'Nucleation of rupture under slip dependent friction law: Simple models of fault zone', *Journal of Geophysical Research: Solid Earth*, 107(B12), p. ESE 2-1-ESE 2-19. doi: 10.1029/2001JB000452.

Ampuero, J. P. (2008a) 'BIMAT-PCSI'. Available at: http://web.gps.caltech.edu/~ampuero/soft/bimat_1.1.2.tar.gz.

Ampuero, J. P. (2008b) 'SBIEMLAB'. Available at: http://web.gps.caltech.edu/~ampuero/soft/SBIEMLAB_0.1.tar.gz.

Ampuero, J. P. and Ben-Zion, Y. (2008) 'Cracks, pulses and macroscopic asymmetry of dynamic rupture on a bimaterial interface with velocity-weakening friction', *Geophysical Journal International*, 173(2), pp. 674–692. doi: 10.1111/j.1365-246X.2008.03736.x.

Ampuero, J. P., Ripperger, J. and Mai, P. M. (2006) 'Properties of dynamic earthquake ruptures with heterogeneous stress drop', *Geophysical Monograph Series*, 170, pp. 255–261. doi: 10.1029/170GM25.

Avouac, J.-P., Meng, L., Wei, S., Wang, T. and Ampuero, J.-P. (2015) 'Lower edge of locked Main Himalayan Thrust unzipped by the 2015 Gorkha earthquake', *Nature Geoscience*. Nature Publishing Group, 8(9), pp. 708–711. doi: 10.1038/ngeo2518.

Azad, M. ., Garagash, D. I. . and Satish, M. (2017) 'Nucleation of dynamic slip on a hydraulically fractured fault', *Journal of Geophysical Research: Solid Earth*. Wiley-Blackwell, 122(4), pp. 2812–2830. doi: 10.1002/2016JB013835.

Bruhat, L. and Segall, P. (2017) 'Deformation rates in northern Cascadia consistent with slow updip propagation of deep interseismic creep', *Geophysical Journal International*. Oxford University Press, 211(1), pp. 427–449. doi: 10.1093/gji/ggx317.

Buijze, L., van den Bogert, P. A. J., Wassing, B. B. T., Orlic, B. and ten Veen, J. (2017) 'Fault reactivation mechanisms and dynamic rupture modelling of depletion-induced seismic events in a Rotliegend gas reservoir', *Netherlands Journal of Geosciences*. Cambridge University Press, 96(05), pp. s131–s148. doi: 10.1017/njg.2017.27.

Day, S. M., Dalguer, L. A., Lapusta, N. and Liu, Y. (2005) 'Comparison of finite difference and boundary integral solutions to three-dimensional spontaneous rupture', *Journal of Geophysical Research: Solid Earth*, 110(12), pp. 1–23. doi: 10.1029/2005JB003813.

Dempsey, D. and Suckale, J. (2016) 'Collective properties of injection-induced earthquake sequences: 1. Model description and directivity bias', *Journal of Geophysical Research: Solid Earth*. Wiley-Blackwell, 121(5), pp. 3609–3637. doi: 10.1002/2015JB012550.

Dunham, E. M. (2007) 'Conditions governing the occurrence of supershear ruptures under slip-weakening friction', *Journal of Geophysical Research: Solid Earth*, 112(7), pp. 1–24. doi: 10.1029/2006JB004717.

Ellsworth, W. L. (2013) 'Injection-Induced Earthquakes', *Science*, 341(6142), pp. 1225942–1225942. doi: 10.1126/science.1225942.

Galis, M., Pelties, C., Kristek, J., Moczo, P., Ampuero, J.-P. and Mai, P. M. (2015) 'On the initiation of sustained slip-weakening ruptures by localized stresses', *Geophysical Journal International*, 200(2), pp. 888–907. doi: 10.1093/gji/ggu436.

Galis, M., Ampuero, J. P., Mai, P. M. and Cappa, F. (2017) 'Induced seismicity provides insight into why earthquake ruptures stop', *Science Advances*, 3(12). doi: 10.1126/sciadv.aap7528.

Garagash, D. I. and Germanovich, L. N. (2012) 'Nucleation and arrest of dynamic slip on a pressurized fault', *Journal of Geophysical Research: Solid Earth*. Wiley-Blackwell, 117(B10). doi: 10.1029/2012JB009209.

Kato, N. (2012) 'Fracture energies at the rupture nucleation points of large interplate earthquakes', *Earth and Planetary Science Letters*. Elsevier, 353–354, pp. 190–197. doi: 10.1016/J.EPSL.2012.08.015.

Lapusta, N., Rice, J. R., Ben-Zion, Y. and Zheng, G. (2000) 'Elastodynamic analysis for slow

tectonic loading with spontaneous rupture episodes on faults with rate- and state-dependent friction', *Journal of Geophysical Research: Solid Earth*. Wiley-Blackwell, 105(B10), pp. 23765–23789. doi: 10.1029/2000JB900250.

Michel, S., Avouac, J.-P., Lapusta, N. and Jiang, J. (2017) 'Pulse-like partial ruptures and high-frequency radiation at creeping-locked transition during megathrust earthquakes', *Geophysical Research Letters*. Wiley-Blackwell, 44(16), pp. 8345–8351. doi: 10.1002/2017GL074725.

Mildon, Z. K., Roberts, G. P., Faure Walker, J. P. and Iezzi, F. (2017) 'Coulomb stress transfer and fault interaction over millennia on non-planar active normal faults: the Mw 6.5–5.0 seismic sequence of 2016–2017, central Italy', *Geophysical Journal International*. Oxford University Press, 210(2), pp. 1206–1218. doi: 10.1093/gji/ggx213.

Moczo, P., Kristek, J. and Galis, M. (2014) *The Finite-Difference Modelling of Earthquake Motions: Waves and Ruptures*. Cambridge University Press.

Morrisey, J. W. and Geubelle, P. H. (1997) 'A numerical scheme for mode III dynamic fracture problems', *Int. J. Num. Meth. Eng.*, 40(7), pp. 1181–1196.

Mulder, F. M. M. (2003) *Modelling of stress development and fault slip in and around a producing gas reservoir*, *PhD Thesis*. Technical University of Delft.

Ripperger, J., Ampuero, J. P., Mai, P. M. and Giardini, D. (2007) 'Earthquake source characteristics from dynamic rupture with constrained stochastic fault stress', *Journal of Geophysical Research: Solid Earth*, 112(4), pp. 1–17. doi: 10.1029/2006JB004515.

Rubin, A. M. and Ampuero, J.-P. (2007) 'Aftershock asymmetry on a bimaterial interface', *Journal of Geophysical Research*, 112(B5), p. B05307. doi: 10.1029/2006JB004337.

Uenishi, K. (2009) 'On the Mechanical Destabilization of a Three-Dimensional Displacement-Softening Plane of Weakness', in *Proceedings of the 38th Symposium on Rock Mechanics, Tokyo, Japan, 8–9 January 2009, Committee on Rock Mechanics, The Japan Society of Civil Engineers, Tokyo, Japan.*, pp. 332–337.

Uenishi, K. (2018) 'Three-dimensional fracture instability of a displacement-weakening planar interface under locally peaked nonuniform loading', *Journal of the Mechanics and*

Physics of Solids, 115, pp. 195–207. doi: 10.1016/J.JMPS.2018.03.012.

Uenishi, K. and Rice, J. R. (2003) 'Universal nucleation length for slip-weakening rupture instability under nonuniform fault loading', *Journal of Geophysical Research: Solid Earth*, 108(B1), p. 2042. doi: 10.1029/2001JB001681.

Van Wees, J.-D., Fokker, P. A., Van Thienen-Visser, K., Wassing, B. B. T., Osinga, S., Orlic, B., Ghouri, S. A., Buijze, L. and Pluymaekers, M. (2017) 'Geomechanical models for induced seismicity in the Netherlands: inferences from simplified analytical, finite element and rupture model approaches', *Netherlands Journal of Geosciences*. Cambridge University Press, 96(05), pp. s183–s202. doi: 10.1017/njg.2017.38.

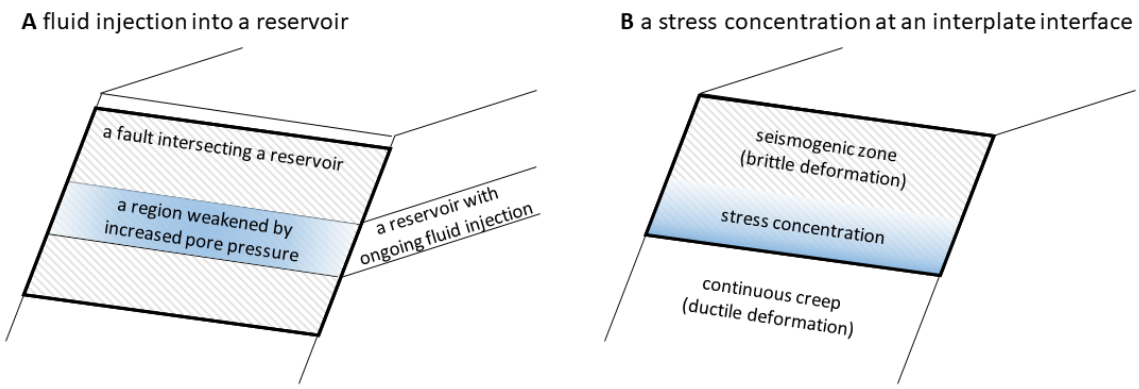

Figure 1 Two examples of situations leading to elongated overstressed asperities. (**A**) A fluid injection into a reservoir intersected by a fault – reservoirs are often much thinner in the vertical direction than horizontally; therefore, their intersection with a sub-vertical fault, weakened by increased pore pressure, is elongated. (**B**) Interplate interface – deep fault creep induces elongated stress concentrations along the bottom of the locked seismogenic zone.

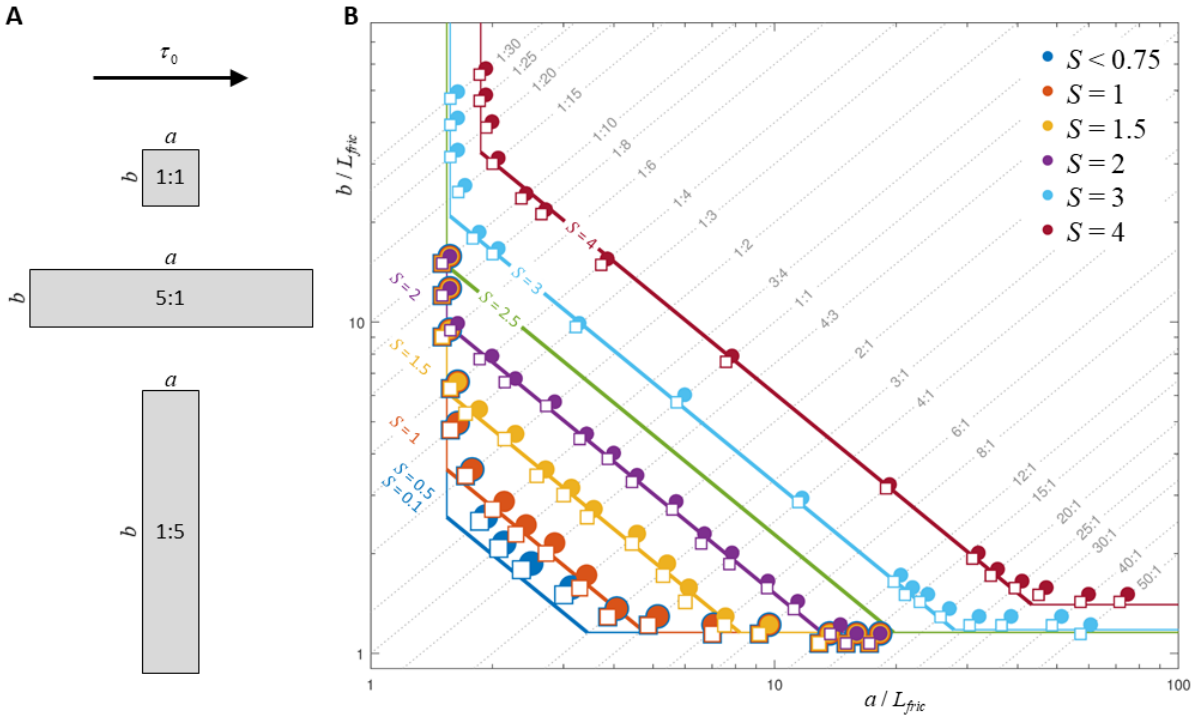

Figure 2 (**A**) Overstressed asperities of different shapes (top to bottom): square, elongated in mode II and in mode III directions with respect to the orientation of the initial traction, τ_o (arrow on top). The asperity sizes a and b correspond to the mode II and mode III edges of the asperity, respectively. (**B**) Comparison of theory and simulations of transition to runaway ruptures as a function of the dimensions of an overstressed asperity and background stress. Empty symbols denote the largest asperities leading to arrested ruptures in our simulations; solid symbols denote the smallest asperities leading to runaway ruptures. Results are colour-coded by their assumed value of the non-dimensional strength parameter S (see legend and coloured labels). Bold diagonal lines indicate the theoretical critical area criterion (Galis *et al.*, 2015), thin vertical and horizontal lines our 2D estimates of critical lengths (Appendix A). Results for $S < 0.75$ are identical, as illustrated by $S = 0.1$ and $S = 0.5$. Dotted diagonal lines are lines of equal aspect ratio (see grey labels).

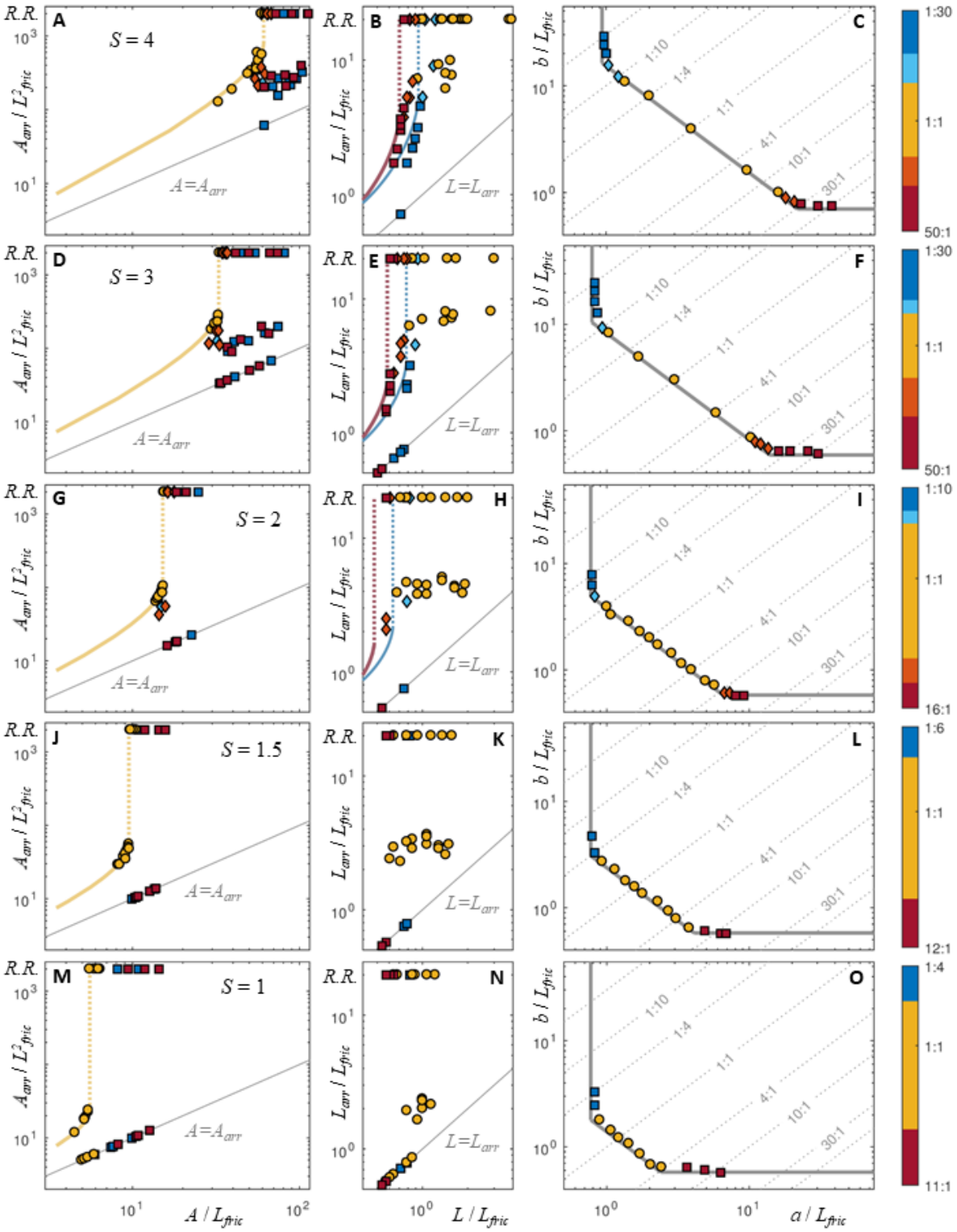

Theoretical estimates
- estimate of arrested area (Galis et al, 2017)
- estimate of arrested length for mode II (Appendix A)
- estimate of arrested length for mode III (Appendix A)

Rupture arrest controlled by
- □ length of asperity (group 1)
- ○ area of asperity (group 2)
- ◇ neither length nor area of asperity (group 3)

Figure 3 Left column: comparison of area of arrested ruptures with theoretical estimate; Middle column: comparison of arrested length with theoretical estimates; Right column: Separation of the three groups in the $a-b$ plot (compare with Fig 2B). Different symbols represent the three groups of behaviour while colour of symbols represent aspect ratios (red and blue tones depict asperities elongated in mode II and III directions, respectively).

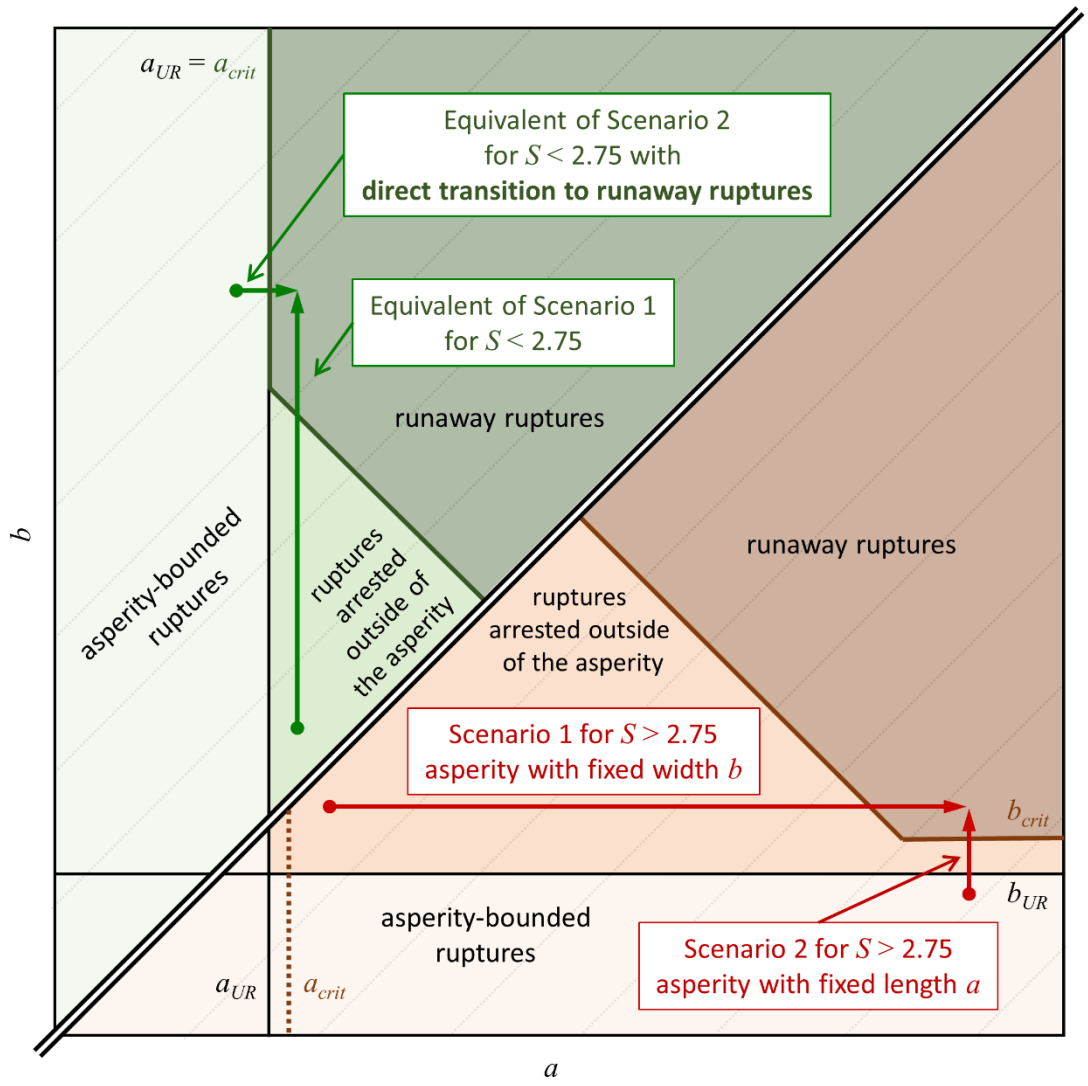

Figure 4 Dependency of rupture modes on asperity size for $S < 2.75$ and aspect ratios smaller than one (upper triangle) and for $S > 2.75$ and aspect ratios greater than one (bottom triangle). This compact representation of both cases exploits the quasi-symmetry of Fig 2B. For $S > 2.75$, scenarios for $b \geq b_{crit}$ are shown (as discussed in the text). For $S < 2.75$, equivalent scenarios for $a \geq a_{crit}$ are shown.

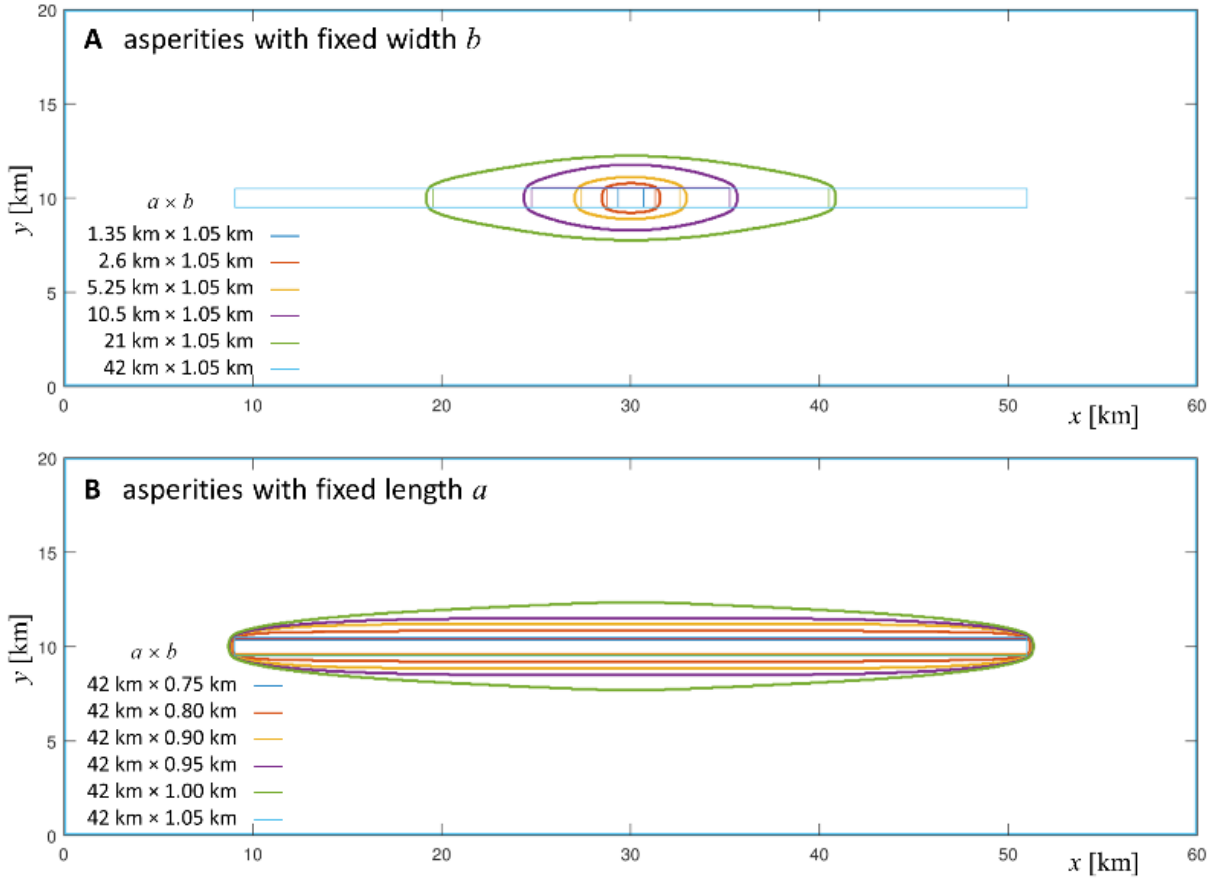

Figure 5 Comparison of ruptures nucleated by asperities with fixed width (**A**) or fixed length (**B**). Asperities are depicted by thin lines and contours of the final size of ruptures by bold lines. The light blue frame indicates the runaway rupture nucleated by asperity with a=42 km and b=1.05 km. The changes of width of the asperities in (**B**) are so small that the asperities are almost indistinguishable.

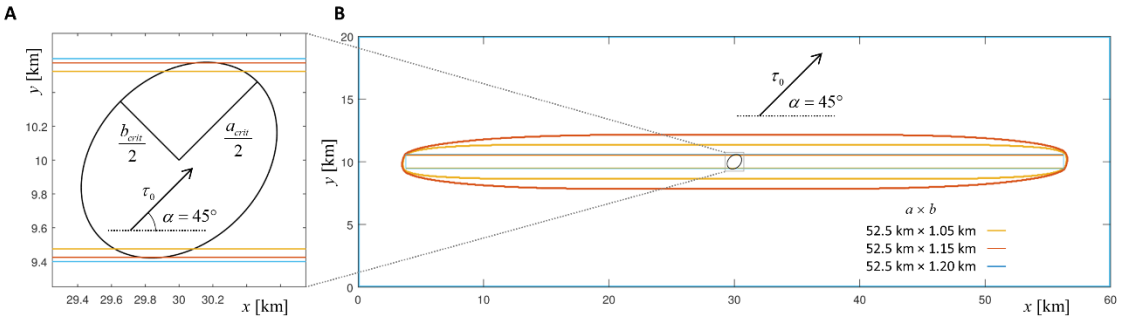

Figure 6 Results of the numerical test for oblique orientation of asperity and initial traction. (**A**) Visual comparison of width of the asperity with the ellipse determined by the critical lengths (a_{crit} and b_{crit}) and orientation of the initial traction τ_0. (**B**) Final sizes of ruptures (bold lines) nucleated by the three considered asperities (thin lines).

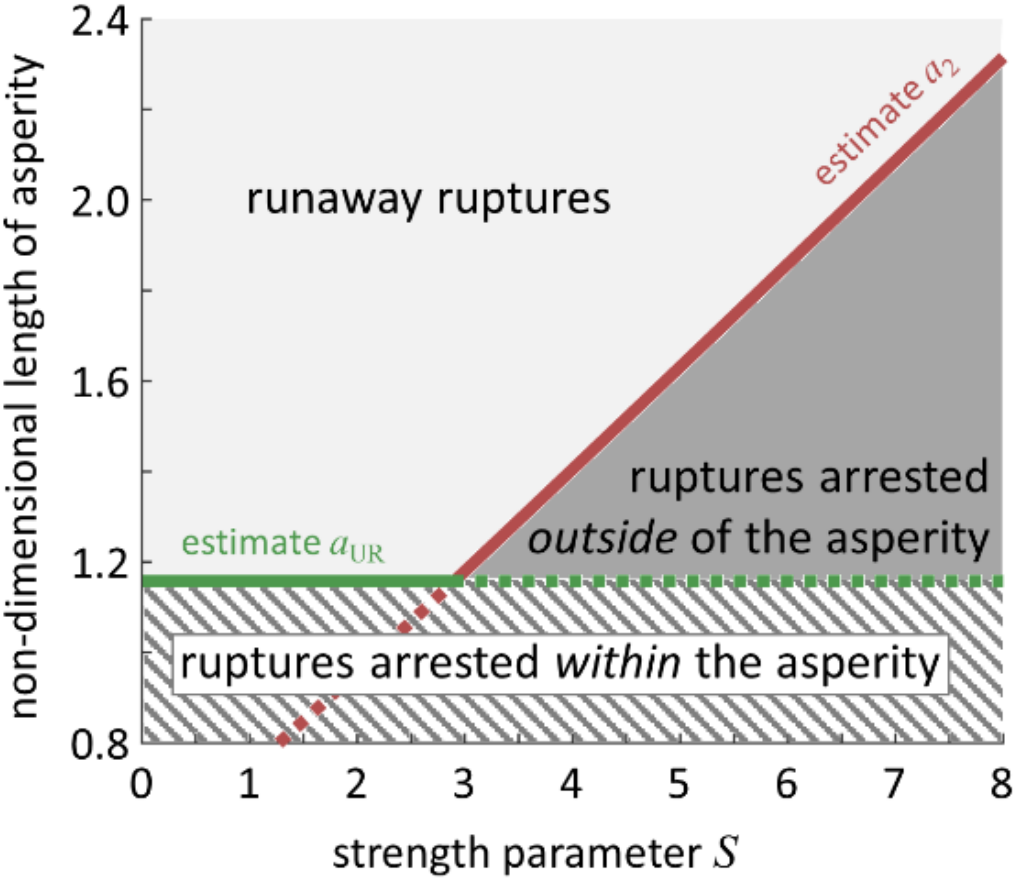

Figure A1 Dependency of critical length $a_c = \max(a_{UR}, a_2)$ on strength parameter S and different rupture regimes in 2D mode III rupture. The asperity length is normalized by $L_{fric} = \mu . D_c / (\tau_s - \tau_d)$.

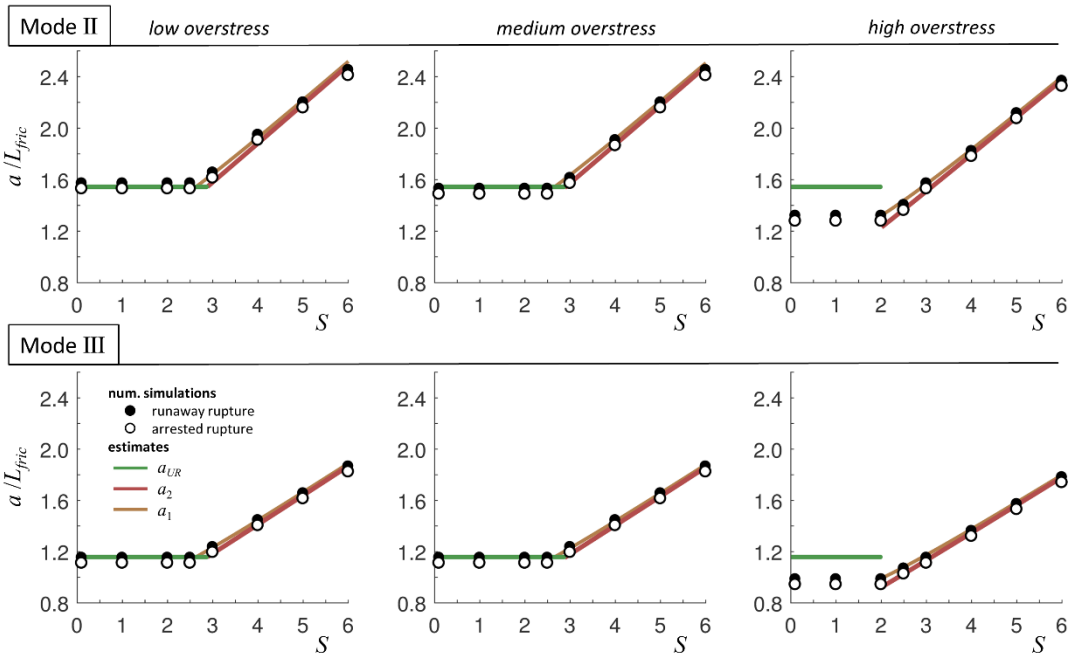

Figure B1 Comparison of the transition to the runaway ruptures observed in numerical simulations (depicted by symbols) with theoretical estimates (depicted by lines) for mode II and mode III ruptures and for three considered levels of the overstress – low (0.0000005% of the strength excess), medium (0.5% of the s.e.) and high (5% of the s.e.). The results are plotted in terms of dimensionless length of the asperity a / L_{fric} (where $L_{fric} = \mu.D_c / (\tau_s - \tau_d)$) as a function of the strength parameter S.

Table B1 Summary of parameter values used for the numerical simulations; σ_0 - initial normal traction, τ_0 - initial shear traction (varied to satisfy the desired value of S), S - strength parameter, μ_s - static friction coefficient, μ_d - dynamic friction coefficient, D_c - characteristic slip-weakening distance, v_s - shear wave speed, ρ - density.

σ_0	τ_0	S	μ_s	μ_d	D_c	v_s	ρ
120 MPa	65.619 – 81.152 MPa	0.1 – 6.0	0.6778	0.525	0.4 m	3464 m/s	2670 kg/m^3